Monthly Notices
of the
ROYAL ASTRONOMICAL SOCIETY

MNRAS **526,** 6004–6014 (2023)
Advance Access publication 2023 October 14

https://doi.org/10.1093/mnras/stad3148

Polarized resonance line transfer in a spherically symmetric medium with angle-dependent partial frequency redistribution

M. Sampoorna[1]★ and H. D. Supriya[2,3]

[1] *Indian Institute of Astrophysics, Koramangala, Bengaluru 560 034, India*
[2] *Instituto de Astrofísica de Canarias, E-38205 La Laguna, Tenerife, Spain*
[3] *Departamento de Astrofísica, Universidad de La Laguna, E-38206 La Laguna, Tenerife, Spain*

Accepted 2023 October 11. Received 2023 October 9; in original form 2023 September 15

ABSTRACT

In a stellar atmosphere, the resonance line polarization arises from scattering of limb-darkened radiation field by atoms. This spectral line polarization gets affected particularly in the wings, when the line photons suffer scattering on electrons in thermal motion. Scattering of line photons by atoms and electrons are, respectively, described by the atomic and Thomson electron scattering redistribution functions, which in general depend on both the frequencies and directions of incident and scattered photons. In this paper, we consider the polarized spectral line formation in spherically symmetric extended and expanding media accounting for the angle-dependent partial frequency redistribution (AD-PRD) in scattering on both atoms and electrons. We solve this computationally demanding polarized transfer problem using an accelerated lambda iteration method and a method based on orders of scattering approach. In the case of expanding spherical medium, the concerned transfer problem is solved in the comoving frame. Because of the computational limitations, we consider optically thin isothermal spherically symmetric media of different extensions for the static case as well as when the velocity fields are present. For the considered model, we show that the AD-PRD effects on the linear polarization profiles are significant and have to be accounted for.

Key words: line: formation – line: profiles – polarization – radiative transfer – scattering – stars: atmospheres.

1 INTRODUCTION

In a scattering event, frequencies and directions of incident and scattered photons in general get intertwined with each other. This angle and frequency coupling is conveniently described by the angle-dependent partial frequency redistribution (AD-PRD) functions (Hummer 1962; Mihalas 1978; Hubeny & Mihalas 2015) in the unpolarized case and by AD-PRD matrices in the polarized case (Domke & Hubeny 1988; Stenflo 1994; Bommier 1997a,b). Numerical solution of the polarized transfer equation including AD-PRD is, however, known to be computationally challenging because of the difficulty involved in evaluating the scattering terms. Despite this complexity, there have been several polarized transfer studies in the literature that included AD-PRD effects (see e.g. Dumont et al. 1977; Faurobert 1987, 1988; Nagendra, Frisch & Faurobert 2002; Sampoorna, Nagendra & Stenflo 2008, 2017; Nagendra & Sampoorna 2011; Sampoorna, Nagendra & Frisch 2011; Anusha & Nagendra 2012; Nagendra & Sampoorna 2012; Supriya et al. 2012, 2013a,b; Sampoorna & Nagendra 2015a,b; del Pino Alemán et al. 2020; Nagendra et al. 2020; Janett et al. 2021; Benedusi et al. 2022, 2023; Anusha 2023). These studies considered either one-, two-, or three-dimensional atmospheres defined in a Cartesian coordinate system. While these are a good representation of stellar atmospheres, they generally do not account for sphericity effects that are particularly important in highly extended atmospheres such as the ones found in early-type hot stars (Hubeny & Mihalas 2015). On the other hand, to a good approximation, highly extended atmospheres are well represented by a spherically symmetric medium. In Sampoorna, Megha & Supriya (2022), we considered scattering on both atoms and electrons along with the polarized resonance line transfer in a spherically symmetric extended as well as expanding atmosphere. However, the scattering computations were done for a simpler case of angle-averaged partial frequency redistribution (AA-PRD). In this study, we investigate the above-said problem by including AD-PRD and highlight its impact on the linear polarization signals.

The outline of this paper is as follows. In Section 2, we present the basic equations. The numerical methods of solution are described in Section 3. Numerical results are presented in Section 4, where the AD-PRD effects on the linear polarization profiles are discussed. Concluding remarks are given in Section 5.

2 BASIC EQUATIONS

In this paper, we consider a one-dimensional spherically symmetric extended and expanding medium. We account for resonance line scattering on a two-level atom and Thomson scattering of line photons by electrons. For both type of scatterings we use the exact AD-PRD matrices. We solve the spherically symmetric polarized transfer equation by the tangent-ray method (Hummer & Rybicki 1971). In this method, the transfer equation is solved along a set of tangent rays defined in the (p, z) coordinate system, where p is the

---

★ E-mail: sampoorna@iiap.res.in

impact parameter of the ray and z is distance along it (see fig. 1 of Megha et al. 2019). Furthermore, we consider the comoving frame (CMF) formulation of the transfer equation (Hubeny & Mihalas 2015). This allows us to take into account the presence of a non-zero non-relativistic radial velocity v_r in the medium. In Section 2.1, we present the CMF transfer equation in the Stokes vector basis and then in Section 2.2, the irreducible spherical tensorial representation, which is well suited for devising efficient numerical schemes (Frisch 2009, 2010).

2.1 Stokes vector representation

The CMF polarized transfer equation in the (p, z) coordinate system and in the non-relativistic limit is given by

$$\pm\frac{\partial \boldsymbol{I}^{\pm}(z,p,\nu)}{\partial \tau(z,\nu)} = \boldsymbol{I}^{\pm}(z,p,\nu) - \boldsymbol{S}(z,p,\nu) - \tilde{\boldsymbol{S}}(z,p,\nu), \tag{1}$$

where $\boldsymbol{I}^{\pm} = (I^{\pm}, Q^{\pm})^{\mathrm{T}}$ denotes the Stokes vector for the incoming '$-$' and the outgoing '$+$' tangent rays, with I representing the specific intensity and Q the linear polarization. The reference direction for positive Q is defined to be perpendicular to the radius vector. The monochromatic optical depth along the tangent ray is given by $\mathrm{d}\tau(z,\nu) = -\chi(r,\nu)\mathrm{d}z$, where ν is the frequency, r is the radius, and $\chi(r,\nu) = \chi_l(r)\varphi(\nu) + \chi_{\mathrm{c}}(r) + \chi_{\mathrm{e}}(r)$ is the total absorption coefficient. The line-integrated absorption coefficient $\chi_l(r)$, continuum absorption coefficient $\chi_{\mathrm{c}}(r)$, and the electron scattering opacity $\chi_{\mathrm{e}}(r)$ are assumed to vary as $1/r^2$ (namely, the inverse square law opacity distribution). The line absorption profile $\varphi(\nu)$ is given by the normalized Voigt function. The total source vector is given by

$$\boldsymbol{S}(z,p,\nu) = \frac{\varphi(\nu)\boldsymbol{S}_l(z,p,\nu) + \beta_c\boldsymbol{S}_c + \beta_e\boldsymbol{S}_e(z,p,\nu)}{\varphi(\nu)+\beta_c+\beta_e}, \tag{2}$$

where $\beta_c = \chi_c/\chi_l$ and $\beta_e = \chi_e/\chi_l$. For scattering on a two-level atom, the line source vector has the form

$$\boldsymbol{S}_l(z,p,\nu) = \epsilon B_{\nu_0}\boldsymbol{U} + \int_0^{\infty} d\nu' \oint \frac{d\Omega'}{4\pi}\frac{\mathbf{R}_{\mathrm{a}}(\nu,\Omega,\nu',\Omega')}{\varphi(\nu)}\boldsymbol{I}(z,\mu',\nu'). \tag{3}$$

Scattering of an incoming ray with frequency ν' and direction $\boldsymbol{\Omega}'$ (θ', ϕ') by a two-level atom into an outgoing ray with frequency ν and direction $\boldsymbol{\Omega}$ (θ, ϕ) is described by the AD-PRD matrix $\mathbf{R}_{\mathrm{a}}$ (see Domke & Hubeny 1988; Bommier 1997a). The explicit form of this matrix is given in equations (1) and (2) of Sampoorna (2014). The ray direction $\boldsymbol{\Omega}$ (θ, ϕ) with θ the inclination and ϕ the azimuth is defined about the local radius vector. In the above equations, $\mu = \cos\theta$. In the (p, z) coordinate system, μ varies along a given impact parameter ray and is given by $\mu(r,p) = \sqrt{1-(p/r)^2}$. Because we do not consider any external magnetic fields and work in the CMF, the polarized radiation field is azimuthally symmetric, so that the Stokes vector depends only on μ. In the above equation, ϵ denotes the thermalization parameter, B_{ν_0} the Planck function at the line centre, and $\boldsymbol{U} = (1, 0)^{\mathrm{T}}$. Since this paper aims to study the effects of AD-PRD on linear polarization profiles formed in spherically symmetric medium, we assume the background continuum to be unpolarized. Consequently, the continuum source vector is of the form $\boldsymbol{S}_c = B_{\nu_0}\boldsymbol{U}$.

The electron scattering source vector is given by

$$\boldsymbol{S}_e(z,p,\nu) = \int_0^{\infty} d\nu' \oint \frac{d\Omega'}{4\pi}\mathbf{R}_{\mathrm{e}}(\nu,\Omega,\nu',\Omega')\boldsymbol{I}(z,\mu',\nu'). \tag{4}$$

The AD-PRD matrix for electron scattering is given by

$$\mathbf{R}_{\mathrm{e}}(\nu,\Omega,\nu',\Omega') = \mathbf{P}_{\mathrm{R}}(\Omega,\Omega')R_{\mathrm{e}}(\nu,\nu',\Theta). \tag{5}$$

Here, $\mathbf{P}_{\mathrm{R}}$ denotes the Rayleigh phase matrix (see Chandrasekhar 1950) and $R_{\mathrm{e}}(\nu,\nu',\Theta)$ the AD-PRD function for scattering of line photons on electrons (see the un-numbered equation in p. 420 of Mihalas 1978, see also equation (38) of Supriya et al. 2012), with Θ representing the scattering angle between the incoming and outgoing rays.

The CMF term represented by $\tilde{\boldsymbol{S}}$ has the following form :

$$\tilde{\boldsymbol{S}}(z,p,\nu) = \gamma(r,p,\nu)\,\frac{\partial \boldsymbol{I}^{\pm}(z,p,\nu)}{\partial\nu}, \tag{6}$$

where

$$\gamma(r,p,\nu) = \frac{\nu_0 v_{\mathrm{th}}}{c\,\chi(r,\nu)}\left[(1-\mu^2)\frac{V}{r} + \mu^2\frac{dV}{dr}\right]. \tag{7}$$

Here, ν_0 is the line-centre frequency, c is the speed of light, v_{th} is the thermal velocity of the atom, and $V = v_r/v_{\mathrm{th}}$. We have assumed v_{th} to be constant throughout the spherical medium.

2.2 Irreducible spherical tensorial representation

Solution of the Stokes vector transfer equation including AD-PRD is known to be computationally very demanding. Therefore, to relatively reduce the computational costs involved, Frisch (2009, 2010) devised a Stokes vector decomposition technique. In this technique, the Stokes and source vectors are decomposed into their irreducible components using the spherical or geometrical tensors (Landi Degl'Innocenti & Landolfi 2004) and an azimuthal Fourier expansion of the AD-PRD functions (Domke & Hubeny 1988). The cosine Fourier series expansion of these functions over the azimuth difference $(\phi - \phi')$ consists of azimuthal Fourier coefficients of different order k, which in general takes values $k = 0, 1, 2, \cdots, \infty$ (see e.g. equation 13 of Frisch 2009). However, in the non-magnetic case, because of the azimuthal symmetry of the radiation field, the azimuthal Fourier coefficients get limited to orders 0, 1, and 2 (see equation 14 of Frisch 2010). This technique originally devised for transfer in planar medium is applied here for transfer in spherical medium.

For convenience, here we consider the component form of the Stokes vector, namely $I_i^{\pm}$ with $i = 0, 1$ representing the specific intensity $I^{\pm}$ and linear polarization $Q^{\pm}$, respectively. Following Frisch (2010), the decomposition of the Stokes vector component $I_i^{\pm}$ into its four irreducible components $\mathcal{I}_Q^{K,\pm}$ can be written as

$$I_i^{\pm}(z,p,\nu) = \sum_{K=0,2}\sum_{Q\geqslant 0}^{K}\tilde{\mathcal{T}}_Q^K(i,\mu)\mathcal{I}_Q^{K,\pm}(z,p,\nu), \qquad i = 0, 1, \tag{8}$$

where $\tilde{\mathcal{T}}_Q^K(i,\mu)$ are the irreducible spherical tensors (Frisch 2010). Similarly, the components of the source vectors S_i, $S_{l,\,i}$, $S_{c,\,i}$, and $S_{e,\,i}$, the CMF term $\tilde{S}_i$, and U_i can also be decomposed into their respective irreducible components $\mathcal{S}_Q^K$, $\mathcal{S}_{l,Q}^K$, $\mathcal{S}_{c,Q}^K$, $\mathcal{S}_{e,Q}^K$, $\tilde{\mathcal{S}}_Q^K$, and $\mathcal{U}_Q^K$. Clearly, $\mathcal{S}_{c,Q}^K = \delta_{K0}\delta_{Q0}B_{\nu_0}$ and $\mathcal{U}_Q^K = \delta_{K0}\delta_{Q0}$. The CMF polarized transfer equation in the irreducible spherical tensor representation can be written as

$$\pm\frac{\partial \boldsymbol{\mathcal{I}}^{\pm}(z,p,\nu)}{\partial\tau(z,\nu)} = \boldsymbol{\mathcal{I}}^{\pm}(z,p,\nu) - \boldsymbol{\mathcal{S}}(z,p,\nu) - \tilde{\boldsymbol{\mathcal{S}}}(z,p,\nu), \tag{9}$$

where the four-component vectors $\boldsymbol{\mathcal{I}}^{\pm} = \left[\mathcal{I}_0^{0,\pm}, \mathcal{I}_0^{2,\pm}, \mathcal{I}_1^{2,\pm}, \mathcal{I}_2^{2,\pm}\right]^{\mathrm{T}}$, $\boldsymbol{\mathcal{S}} = \left[\mathcal{S}_0^0, \mathcal{S}_0^2, \mathcal{S}_1^2, \mathcal{S}_2^2\right]^{\mathrm{T}}$, and $\tilde{\boldsymbol{\mathcal{S}}} = \left[\tilde{\mathcal{S}}_0^0, \tilde{\mathcal{S}}_0^2, \tilde{\mathcal{S}}_1^2, \tilde{\mathcal{S}}_2^2\right]^{\mathrm{T}}$. Following Supriya et al. (2012), we combine line and electron source vectors into a single source vector $\boldsymbol{\mathcal{S}}_L$ given by

$$\boldsymbol{\mathcal{S}}_L(z,p,\nu) = \epsilon B_{\nu_0}\boldsymbol{\mathcal{U}} + \overline{\boldsymbol{\mathcal{J}}}(z,p,\nu), \tag{10}$$

where $\boldsymbol{\mathcal{U}} = [1, 0, 0, 0]^{\mathrm{T}}$, and the scattering integral has the form

$$\overline{\boldsymbol{\mathcal{J}}}(z, p, \nu) = \int_0^\infty d\nu' \int_{-1}^{+1} \frac{d\mu'}{2} \frac{\tilde{\boldsymbol{\mathcal{R}}}(\nu, \mu, \nu', \mu')}{\varphi(\nu)} \tilde{\Gamma}(\mu') \boldsymbol{\mathcal{I}}(z, \mu', \nu'). \tag{11}$$

The elements of the 4 × 4 matrix $\tilde{\Gamma}$ is given in appendix of Frisch (2010). The 4 × 4 matrix $\tilde{\boldsymbol{\mathcal{R}}}$ is diagonal, namely, $\tilde{\boldsymbol{\mathcal{R}}} = \mathrm{diag}\left[\tilde{\mathcal{R}}^0_0, \tilde{\mathcal{R}}^2_0, \tilde{\mathcal{R}}^2_1, \tilde{\mathcal{R}}^2_2\right]$, where the diagonal elements are of the form

$$\tilde{\mathcal{R}}^0_0 = \alpha \tilde{r}^{(0)}_{\mathrm{II}} + \left[\beta^{(0)} - \alpha\right] \tilde{r}^{(0)}_{\mathrm{III}} + \beta_e \tilde{r}^{(0)}_e, \tag{12}$$

$$\tilde{\mathcal{R}}^2_Q = W_2 \left\{\alpha \tilde{r}^{(Q)}_{\mathrm{II}} + \left[\beta^{(2)} - \alpha\right] \tilde{r}^{(Q)}_{\mathrm{III}}\right\} + \beta_e \tilde{r}^{(Q)}_e, \quad Q = 0, 1, 2, \tag{13}$$

where W_2 is the atomic polarizability factor (which is unity for a normal Zeeman triplet considered here). The symbol $\tilde{r}^{(Q)}_{\mathrm{X}}$ with X= II, III, or e, respectively, represent the Qth-order azimuthal Fourier coefficients of the type-II and type-III AD-PRD functions of Hummer (1962) and of $R_e(\nu, \nu', \Theta)$. They are given by

$$\tilde{r}^{(Q)}_{\mathrm{X}}(\nu, \mu, \nu', \mu') = \frac{2 - \delta_{0Q}}{2\pi} \times \int_0^{2\pi} R_{\mathrm{X}}(\nu, \mu, \nu', \mu', \phi - \phi') \cos[Q(\phi - \phi')] d(\phi - \phi'). \tag{14}$$

The branching ratios α and $\beta^{(K)}$ are of the form (Bommier 1997a)

$$\alpha = \frac{\Gamma_R}{\Gamma_R + \Gamma_I + \Gamma_E}, \tag{15}$$

$$\beta^{(K)} = \frac{\Gamma_R}{\Gamma_R + \Gamma_I + D^{(K)}}, \tag{16}$$

where Γ_R is the radiative deexcitation rate, Γ_I and Γ_E are, respectively, the inelastic deexcitation and elastic collisional rates, and $D^{(K)}$ the collisional depolarization rate (with $D^{(0)} = 0$).

In the irreducible spherical tensor representation, the total source vector takes the following form:

$$\boldsymbol{\mathcal{S}}(z, p, \nu) = \frac{\varphi(\nu)\boldsymbol{\mathcal{S}}_L(z, p, \nu) + \beta_c \boldsymbol{\mathcal{S}}_c}{\varphi(\nu) + \beta_c + \beta_e}, \tag{17}$$

where $\boldsymbol{\mathcal{S}}_c = B_{\nu_0}\boldsymbol{\mathcal{U}}$. The CMF term $\tilde{\boldsymbol{\mathcal{S}}}$ in the irreducible spherical tensor representation has the same form given in equation (6), but with $\boldsymbol{\mathcal{I}}^{\pm}$ in place of $\boldsymbol{I}^{\pm}$.

3 NUMERICAL METHODS OF SOLUTION

In this section, we describe the solution to the CMF polarized transfer equation (9) using two different iterative schemes namely, polarized accelerated lambda iteration method (see Section 3.1) and scattering expansion method (see Section 3.2). The latter method is preferred from a computational point of view.

3.1 The polarized accelerated lambda iteration

An iterative method begins with a guess value for the unknown, namely the irreducible source vector $\boldsymbol{\mathcal{S}}(z, p, \nu)$, followed by a call to the formal solver to compute the irreducible Stokes vector $\boldsymbol{\mathcal{I}}^{\pm}(z, p, \nu)$ and subsequently an updated value of $\boldsymbol{\mathcal{S}}(z, p, \nu)$. This process is repeated until the solution converges. It is well-known that such an iterative method is prone to very slow or even no convergence especially for optically thick scattering dominated media (Hubeny & Mihalas 2015). This difficulty is overcome by accelerating the convergence via the so-called operator splitting methods (Cannon 1973). These methods are known as accelerated lambda iteration (ALI). ALI methods have been applied to a wide variety of problems, both unpolarized (Hubeny & Mihalas 2015) and polarized (see the reviews by Trujillo Bueno 2003; Nagendra 2019a,b).

Formal solution of the polarized transfer equation (9) can be written symbolically as

$$\boldsymbol{\mathcal{I}}^{\pm}(p, \nu) = \boldsymbol{\Lambda}^{\pm}(p, \nu)[\boldsymbol{\mathcal{S}}(p, \nu) + \tilde{\boldsymbol{\mathcal{S}}}(p, \nu)] + \boldsymbol{T}^{\pm}(p, \nu), \tag{18}$$

where the directly transmitted part of the four-component Stokes vector is denoted by $\boldsymbol{T}^{\pm}(p, \nu)$. For a given impact parameter p and frequency ν the $4N_d \times 4N_d$ integral operator is denoted by $\boldsymbol{\Lambda}^{\pm}(p, \nu)$, where N_d is the total number of depth points. The elements of this lambda operator is determined by the optical distances between the grid points along the depth. A short-characteristic method (Olson & Kunasz 1987) modified to treat the CMF term (Hauschildt & Baron 2004) is used to find the formal solution. For the problem at hand, the explicit form of this CMF short-characteristic formal solution can be found in Sampoorna, Megha & Supriya (2022, see their section 2).

An iterative scheme is set up via

$$\boldsymbol{\mathcal{S}}^{n+1}(p, \nu) = \boldsymbol{\mathcal{S}}^n(p, \nu) + \delta\boldsymbol{\mathcal{S}}^n(p, \nu), \tag{19}$$

where n is the index of iteration and $\delta\boldsymbol{\mathcal{S}}^n$ is the source vector correction. A similar expression can be written for the combined source vector $\boldsymbol{\mathcal{S}}_L$. As for the CMF term $\tilde{\boldsymbol{\mathcal{S}}}$, since it is evaluated within the formal solver at each iteration, an iterative correction is unnecessary (Megha et al. 2020). Now using the operator splitting technique, namely, $\boldsymbol{\Lambda} = \boldsymbol{\Lambda}^* + (\boldsymbol{\Lambda} - \boldsymbol{\Lambda}^*)$ wherein $\boldsymbol{\Lambda}^*$ is a diagonal approximate operator (Olson, Auer & Buchler 1986), we obtain for the combined source vector correction the following expression :

$$\begin{aligned}\delta\boldsymbol{\mathcal{S}}^n_L(p, \nu) - \int_0^\infty d\nu' \int_{-1}^{+1} \frac{d\mu'}{2} \frac{\tilde{\boldsymbol{\mathcal{R}}}(\nu, \mu, \nu', \mu')}{\varphi(\nu)} \tilde{\Gamma}(\mu') \\ \times \frac{\chi_l(r)\varphi(\nu')}{\chi(r, \nu')} \boldsymbol{\Lambda}^*(\mu', \nu') \left[\delta\boldsymbol{\mathcal{S}}^n_L(\mu', \nu')\right] \\ = \boldsymbol{r}^n(p, \nu),\end{aligned} \tag{20}$$

where the residual vector $\boldsymbol{r}^n(p, \nu) = \epsilon B_{\nu_0}\boldsymbol{\mathcal{U}} + \overline{\boldsymbol{\mathcal{J}}}^n(p, \nu) - \boldsymbol{\mathcal{S}}^n_L(p, \nu)$. The scattering integral $\overline{\boldsymbol{\mathcal{J}}}^n$ at the nth iterate is obtained from the formal solver using the nth iterate source vector. The linear system of equations (20) for the combined source vector corrections can be recast in the following form :

$$\mathbf{A}\, \delta\boldsymbol{\mathcal{S}}^n_L = \boldsymbol{r}^n, \tag{21}$$

where at each depth point, $\boldsymbol{r}^n$ and $\delta\boldsymbol{\mathcal{S}}^n_L$ are vectors of length $4N_\nu 2N_\mu$ and $\mathbf{A}$ is a matrix of size $4N_\nu 2N_\mu \times 4N_\nu 2N_\mu$. The total number of frequency points is denoted by N_ν, while N_μ denotes the number of angle points in the range $[0 < \mu \leqslant 1]$. We solve this linear system of equations using a frequency-angle by frequency-angle method described in Sampoorna, Nagendra & Frisch (2011, see also Supriya et al. 2012). In the case of spherical transfer in (p, z) coordinate system, not all the impact parameter rays intersect a given spherical shell. While all the rays intersect the outermost spherical shell, only the core rays intersect the innermost spherical shell. This is expected because impact parameter rays are defined to be tangent to spherical shells (see fig. 1 of Megha et al. 2019). Thus the number of rays intersecting a given spherical shell varies with the depth point. In other words N_μ varies with the depth point. For example, if N_c denotes the number of core rays, then $N_\mu = N_c$ for the innermost spherical shell, while $N_\mu = N_c + N_d$ for the outermost spherical shell. Therefore, the size of linear system of equations (21) changes from one depth point to the other and is much larger than that in the corresponding planar case. As a result, the computational costs involved in solving equation (21) using the frequency-angle by frequency-angle method is significantly larger than in the planar case. To somewhat reduce the computational costs, in the following subsection we present the so-called scattering expansion method.

3.2 The scattering expansion method

This iterative method was originally proposed in Frisch et al. (2009) for polarized transfer in planar medium with complete frequency redistribution and turbulent magnetic fields. Here, a Neumann series expansion of the polarized component of the source vector in the mean number of scattering events allows to include the contribution of multiple scatterings iteratively. The intensity component of the source vector is computed with an ALI method neglecting its coupling with the linear polarization. This scattering expansion method has been generalized to both AA-PRD and AD-PRD problems with and without weak magnetic fields in a planar medium (see the reviews by Nagendra 2019a,b). More recently, this method has been extended to polarized transfer in arbitrary magnetic fields with AA-PRD (Sampoorna et al. 2019) and AD-PRD (Nagendra et al. 2020). Here, we apply this iterative method to polarized line transfer in a spherical medium with AD-PRD.

In the component form, the combined source vector given in equation (10) can be re-written as

$$\mathcal{S}^K_{L,Q}(z,p,\nu) = \epsilon B_{\nu_0}\mathcal{U}^K_Q + \overline{\mathcal{J}}^K_Q(z,p,\nu), \tag{22}$$

where

$$\overline{\mathcal{J}}^K_Q(z,p,\nu) = \int_0^\infty d\nu' \int_{-1}^{+1} \frac{d\mu'}{2} \frac{\tilde{\mathcal{R}}^K_Q(\nu,\mu,\nu',\mu')}{\varphi(\nu)} \times \sum_{K'=0,2} \sum_{Q'\geqslant 0}^{K'} \tilde{\Gamma}^{KK'}_{QQ'}(\mu')\mathcal{I}^{K'}_{Q'}(z,\mu',\nu'). \tag{23}$$

As already mentioned, we first compute the intensity $I^{\pm}(z,\ p,\ \nu)$ by neglecting its coupling to linear polarization. In other words we assume the Stokes $I^{\pm}(z,\ p,\ \nu)$ to be given by the component $\mathcal{I}^{0,\pm}_0(z,p,\nu)$. The corresponding combined source function $\mathcal{S}^0_{L,0}(z,p,\nu) = \epsilon B_{\nu_0} + \overline{\mathcal{J}}^0_0(z,p,\nu)$, where

$$\overline{\mathcal{J}}^0_0(z,p,\nu) = \int_0^\infty d\nu' \int_{-1}^{+1} \frac{d\mu'}{2} \frac{\tilde{\mathcal{R}}^0_0(\nu,\mu,\nu',\mu')}{\varphi(\nu)} \mathcal{I}^0_0(z,\mu',\nu'). \tag{24}$$

In the above equation, we have neglected the coupling to other $\mathcal{I}^2_Q$ components and used $\tilde{\Gamma}^{00}_{00}(\mu') = 1$ (see appendix of Frisch 2010). The component $\mathcal{I}^{0,\pm}_0(z,p,\nu)$ and $\mathcal{S}^0_{L,0}(z,p,\nu)$ are obtained by solving the scalar version of the transfer equation (9) using the CMF ALI method described in Section 3.1. In this case, for a given depth point the size of the vectors $\boldsymbol{r}^n$ and $\delta\boldsymbol{\mathcal{S}}^n_L$ reduces to $N_\nu 2N_\mu$ and that of matrix $\mathbf{A}$ to $N_\nu 2N_\mu \times N_\nu 2N_\mu$. Clearly, solving this scalar version of the linear system of equations is computationally less demanding than the vector version.

Once the $\mathcal{I}^{0,\pm}_0(z,p,\nu)$ and $\mathcal{S}^0_{L,0}(z,p,\nu)$ are available, the other $K = 2$ and $Q = 0,\ 1,\ 2$ components are computed iteratively as described below. In the first iteration, since only $K = 0$ and $Q = 0$ components are known, equation (23) for $K = 2$ and $Q = 0,\ 1,\ 2$ reduces to

$$\left[\overline{\mathcal{J}}^2_Q\right]^{(1)}(z,p,\nu) \simeq \int_0^\infty d\nu' \int_{-1}^{+1} \frac{d\mu'}{2} \frac{\tilde{\mathcal{R}}^2_Q(\nu,\mu,\nu',\mu')}{\varphi(\nu)} \times \tilde{\Gamma}^{20}_{Q0}(\mu')\mathcal{I}^0_0(z,\mu',\nu'). \tag{25}$$

The above equation basically represents the single scattering contribution to the scattering integral, which is indicated with a superscript (1). A call to the CMF formal solver would then provide the radiation field $\left[\mathcal{I}^{2,\pm}_Q\right]^{(1)}$ corresponding to $\left[\mathcal{S}^2_Q\right]^{(1)}$. Clearly, in the second iteration all the $(K,\ Q)$ components of Stokes and source vectors are available. Thus, all the terms on the right hand side of equation (23) for $K = 2$ can be determined. This process is repeated to derive an iterative sequence, where, in each iteration higher orders of scattering are included. This iterative sequence for the *n*th iteration (or scattering) can be written as

$$\left[\overline{\mathcal{J}}^2_Q\right]^{(n)}(z,p,\nu) \simeq \left[\overline{\mathcal{J}}^2_Q\right]^{(1)}(z,p,\nu) + \int_0^\infty d\nu' \int_{-1}^{+1} \frac{d\mu'}{2} \frac{\tilde{\mathcal{R}}^2_Q(\nu,\mu,\nu',\mu')}{\varphi(\nu)} \times \sum_{Q'\geqslant 0}^{2} \tilde{\Gamma}^{22}_{QQ'}(\mu')\left[\mathcal{I}^2_{Q'}\right]^{(n-1)}(z,\mu',\nu'). \tag{26}$$

Iterations are stopped when the solution converges. For our computations, we adopt the same convergence criteria defined in section 5 of Sampoorna, Nagendra & Frisch (2011).

4 NUMERICAL RESULTS

In this section, we illustrate the AD-PRD effects on the linear polarization profiles emerging from a spherically symmetric isothermal medium. We parametrize this medium by a set of input parameters, namely, $R, T, a, \epsilon, \beta_c$, and β_e. The extension of the spherical medium is specified via an outer radius R that is measured in units of the core radius $R_{\rm core}$. Here, we consider low ($R = 2$), mid ($R = 20$), and highly ($R = 200$) extended spherical media. Furthermore, the extended spherical medium is characterized by a frequency integrated total radial line optical thickness of T. We recall that the underlying line-integrated absorption coefficient is assumed to fall off like $1/r^2$, which is also the case for the continuum absorption coefficient as well as the electron scattering opacity. Because of the computational limitations, here we consider only optically thin cases of $T = 10$ and $T = 100$. For the same reason, here we do not consider the effects of a depolarizing elastic collisions, namely, $D^{(2)} = 0$ and also $\Gamma_E = 0$. In other words, we consider only type-II AD-PRD function. We take the damping width of the Voigt profile to be $a = 10^{-3}$. As in Sampoorna, Megha & Supriya (2022), the ratio of electron to atomic Doppler width is taken to be 43. For the optically thin cases considered here, we use a reflecting boundary condition, namely, $\boldsymbol{\mathcal{I}}^+(\tau = T,p,\nu) = \boldsymbol{\mathcal{I}}^-(\tau = T,p,\nu)$ for all the rays. For the rays that intersect the core, namely the core rays, this condition is applied at $r = R_{\rm core}$, while for all the other rays, called lobe rays, this condition is applied at the spherical shell where the ray is tangent to it. The reflecting boundary for the core rays implies that the central core is hollow and non-emitting. This is equivalent to a finite planar slab that is symmetric about its mid-plane. Furthermore, we assume that there is no radiation incident on the top boundary, namely, $\boldsymbol{\mathcal{I}}^-(\tau = 0,p,\nu) = 0$. Finally, we recall that in the tangent-ray method the direction cosine μ depends on p and r, namely $\mu = \mu(r,p)$ (see the discussion below equation 3). In all the figures presented in this paper, the line-of-sight $\mu_{\rm los}$ at which the emergent Stokes profiles are illustrated corresponds to μ at $r = R$. Since each of the impact parameter ray p emerges at $r = R$ with a unique value of μ, the $\mu_{\rm los} = \mu(R,p)$ corresponds to a unique p.

Figs 1 and 2 show the behaviour of emergent I and Q/I profiles as a function of the logarithm of non-dimensional frequency x (which is defined as $x = (\nu - \nu_0)/\Delta\nu_{\rm D}$, with ν_0 and $\Delta\nu_{\rm D}$, respectively, representing the line-centre frequency and atomic Doppler width). The profiles computed using the AD-PRD are shown as black solid

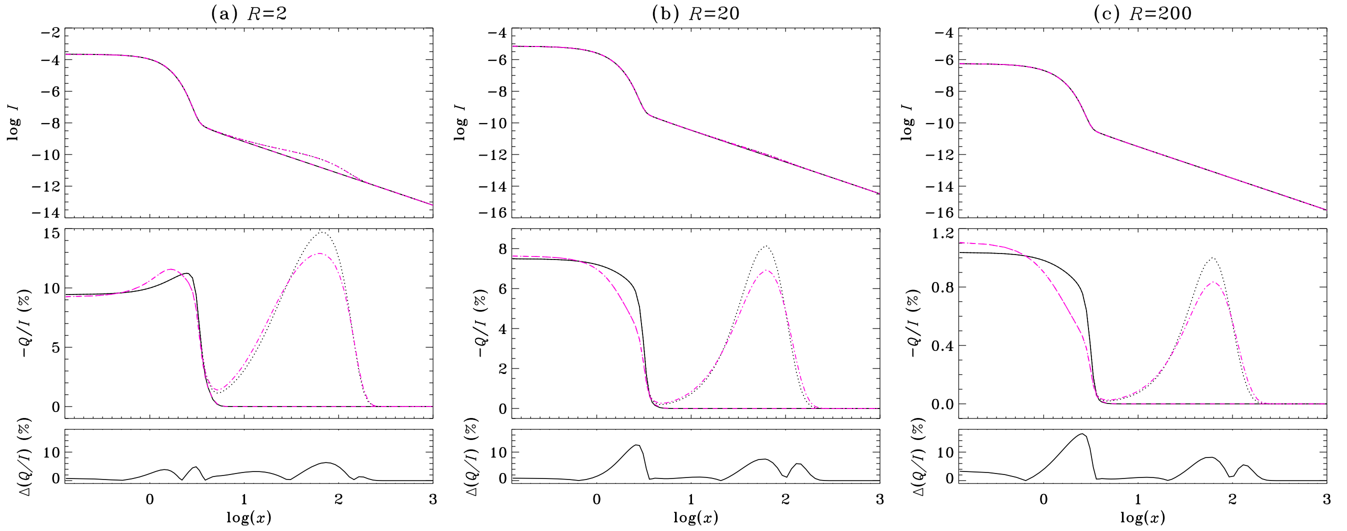

Figure 1. A comparison of the emergent Stokes I and fractional linear polarization Q/I profiles at $\mu_{\rm los} = 0.1$ computed using AD-PRD (black solid and dotted lines) and AA-PRD (pink dashed and dot–dashed lines) functions. Bottom row displays the error $\Delta(Q/I)$ in percentage (see equation 27) when electron scattering is included. A spherically symmetric static medium with line integrated radial optical thickness of $T = 10$ is considered. Panels (a), (b), and (c) correspond, respectively, to $R = 2$, 20, and 200. Other model parameters are $\beta_c = 0$, $\epsilon = 10^{-4}$, $a = 10^{-3}$, and $\Gamma_{\rm E} = 0$. Electron scattering opacity $\beta_e = 0$ for black solid and pink dashed lines, while it is 10^{-5} for black dotted and pink dot–dashed lines. Black solid and dotted lines coincide in the line core (namely, $\log(x) < 0.5$) and near wing (namely, $0.5 < \log(x) < 1$) regions of Q/I (middle row). This is also the case for pink dashed and dot–dashed lines. As for the I profiles (upper row), all the different lines coincide in panels (b) and (c), while black solid and pink dashed, and black dotted and pink dot–dashed lines coincide in panel (a).

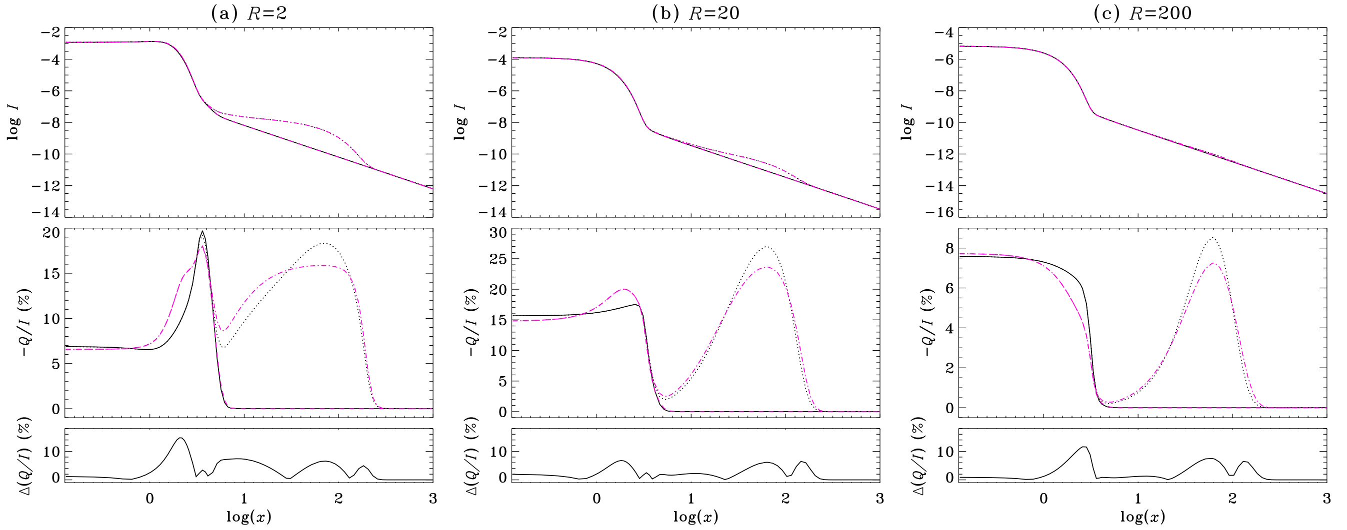

Figure 2. Same as Fig. 1, but for $T = 100$.

and dotted lines, while those computed using AA-PRD are shown as pink dashed and dot–dashed lines. These line sets in-turn also highlight the effects of including (black dotted and pink dot–dashed lines) and neglecting (black solid and pink dashed lines) electron scattering. A spherically symmetric static media with outer radius $R = 2$ (panel (a)), $R = 20$ (panel (b)), and $R = 200$ (panel (c)) are considered. In this case, the Stokes profiles are symmetric about the line centre, and hence only the profiles corresponding to $x > 0$ are shown. In Figs 1 and 2, the line integrated radial optical thickness T is 10 and 100, respectively. The AD-PRD solutions are computed using the scattering expansion method presented in Section 3.2, as it is computationally less demanding than the polarized ALI method discussed in Section 3.1, although both the methods give identical results. The AA-PRD solutions are computed using the polarized ALI method discussed in Sampoorna, Megha & Supriya (2022). In the bottom rows of Figs 1 and 2, we also plot the error $\Delta(Q/I)$ in percentage. Following Riva et al. (2023), we define this error as

$$\Delta(Q/I) = \frac{|X/(\max X) - Y/(\max X)|}{1 + |X/(\max X)|}, \tag{27}$$

where X stands for Q/I obtained using AD-PRD and Y stands for Q/I obtained using AA-PRD.

The effect of electron scattering redistribution on I and Q/I profiles is morphologically similar for AA-PRD and AD-PRD solutions, namely it gives rise to a bulge in the wings of the intensity profile and a far wing secondary peak in the Q/I profiles (compare black solid and dotted lines as well as pink dashed and dot–dashed lines). For an optically thin spherical medium considered here, electron scattering

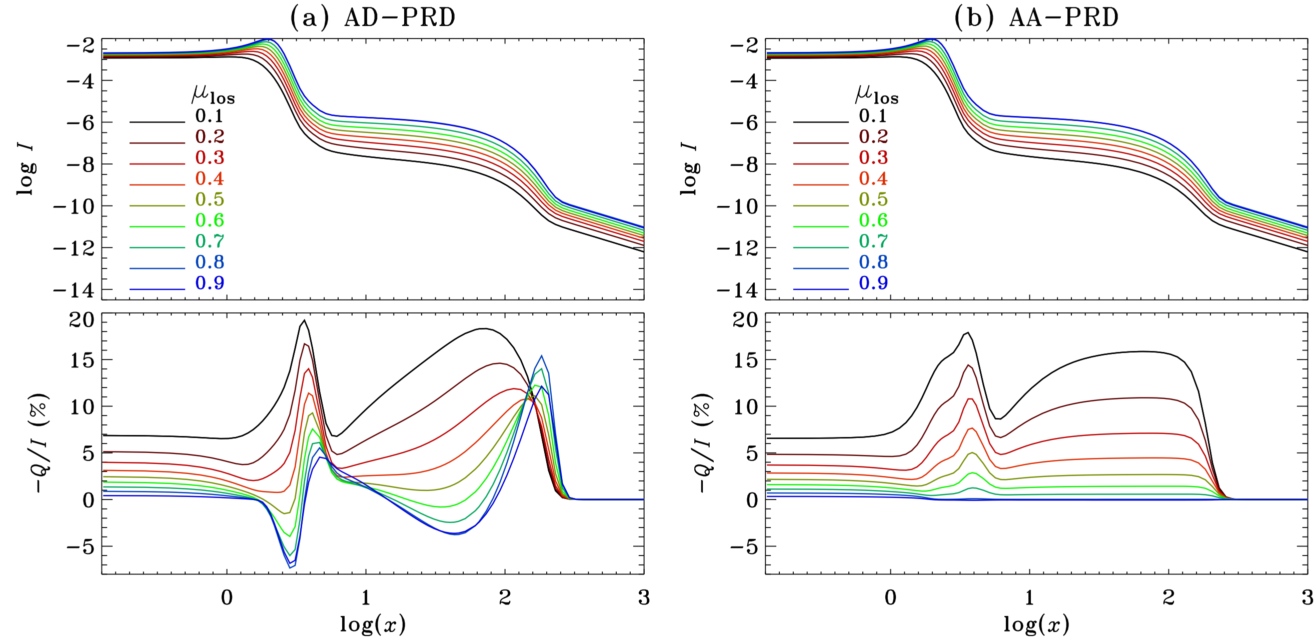

Figure 3. Centre-to-limb variation of the emergent Stokes *I* and fractional linear polarization *Q*/*I* profiles computed using AD-PRD (panel (a)) and AA-PRD (panel (b)) functions. A spherically symmetric static medium with input parameters $R = 2$, $T = 100$, $\beta_c = 0$, $\beta_e = 10^{-5}$, $\epsilon = 10^{-4}$, $a = 10^{-3}$, and $\Gamma_{\rm E} = 0$ is considered. Different lines correspond to a different value of $\mu_{\rm los}$, which is indicated in figure legend.

does not affect the near wing PRD peak (see also Sampoorna, Megha & Supriya 2022), and hence the black solid (pink dashed) and black dotted (pink dot–dashed) lines coincide in the line core and near wing regions. Here, the line core region corresponds to $\log(x) < 0.5$, the near wing region where the near wing PRD peak is seen corresponds to $0.5 < \log(x) < 1$, and the far wing region where the secondary peak is seen corresponds to $1 < \log(x) < 2.5$. The dependence of the *I* and *Q*/*I* profiles on the outer radius *R* is also similar for AD-PRD and AA-PRD cases. We refer the reader to Sampoorna, Megha & Supriya (2022), wherein the nature of this dependence has been discussed for the $T = 100$ case (see their figs 2(a)–4(a) and the related discussions). Unlike the case of $T = 100$, the *Q*/*I* monotonically decreases with increasing *R* for $T = 10$ because the spherical medium becomes highly dilute.

Like in the planar case, the differences between AD-PRD and AA-PRD solutions are mainly seen in the fractional linear polarization profiles. For $R = 2$, noticeable differences in the shape and amplitude of *Q*/*I* are seen at the near wing PRD peak (compare black solid and pink dashed lines in panel (a) of Figs 1 and 2) and the secondary peak (compare black dotted and pink dot–dashed lines in panel (a) of Figs 1 and 2). Small differences in amplitude of *Q*/*I* near the line centre are also seen (see the bottom row in panel (a) of Figs 1 and 2). These differences continue to remain for larger values of *R*, although the near wing PRD peak is highly reduced or nearly non-existent for larger *R* (see panels (b) and (c) of Figs 1 and 2). For $T = 10$, the difference in amplitude of *Q*/*I* near the line centre increases with *R* (see bottom row in Fig. 1), while for $T = 100$ this difference first increases for $R = 20$ and then decreases when $R = 200$ (see bottom row in Fig. 2).

4.1 Centre-to-limb variations

In Figs 3 and 4, we show the centre-to-limb variation of emergent *I* and *Q*/*I* profiles computed with AD-PRD (panel (a)) and AA-PRD (panel (b)), for $T = 100$ and $R = 2$ and $R = 20$, respectively. The different lines-of-sight $\mu_{\rm los}$ at which these profiles are illustrated represent the cosine of the angle made by the impact parameter ray *p* with the outermost spherical shell, namely $\mu_{\rm los} = \mu(R, p)$. Clearly, different values of $\mu_{\rm los}$ basically correspond to different values of the impact parameter *p*. As expected, when the line of sight changes from close to the limb ($\mu_{\rm los} = 0.1$) to near disc centre ($\mu_{\rm los} = 0.9$), *I* profiles exhibit limb-darkening and *Q*/*I* profiles show limb-brightening. The *Q*/*I* computed with AA-PRD monotonically decreases towards zero polarization with increasing values of $\mu_{\rm los}$. However, the *Q*/*I* computed with AD-PRD exhibits this behaviour only in a region close to the line centre (namely, for $\log(x) < 0.2$), while the regions to the left of near wing PRD peak (namely, for $0.2 < \log(x) < 0.6$) and to the left of the secondary peak (namely, for $1.1 < \log(x) < 2.1$) exhibit negative polarization. Furthermore, the near wing PRD peak and the secondary peak themselves are shifted to larger frequencies (see e.g. green and blue lines in panel (a) of Figs 3 and 4). As *R* increases the $\mu_{\rm los}$ at which negative polarization starts to be seen in *Q*/*I* also increases. For example, for $R = 2$ this occurs at $\mu_{\rm los} = 0.5$ (see panel (a) of Fig. 3), for $R = 20$ at $\mu_{\rm los} = 0.7$ (see panel (a) of Fig. 4), while for $R = 200$ it occurs at $\mu_{\rm los} = 0.8$ (figure not illustrated). In other words, the differences in *Q*/*I* computed with AD-PRD and AA-PRD functions is relatively larger for a $\mu_{\rm los}$ close to the disc centre than near the limb (e.g. compare green and blue lines in panels (a) and (b) of Figs 3 and 4). This is in contrast to the planar medium, wherein the differences between AD-PRD and AA-PRD solutions decrease with increasing values of $\mu_{\rm los}$ (see e.g. fig. 8 of Sampoorna, Nagendra & Frisch 2011). This relatively large difference between AD-PRD and AA-PRD solutions can be attributed to the spherical nature of the problem. In a spherical medium, along a given impact parameter ray, $\mu(r, p)$ changes from 0 at an inner spherical shell where the ray is tangent to it to the corresponding emergent $\mu_{\rm los} = \mu(R, p)$ value, thereby enhancing the AD-PRD effects for a larger emergent $\mu_{\rm los}$ value than the smaller one.

To better understand the differences between AD-PRD and AA-PRD solutions, we show in Fig. 5 a comparison of the corresponding

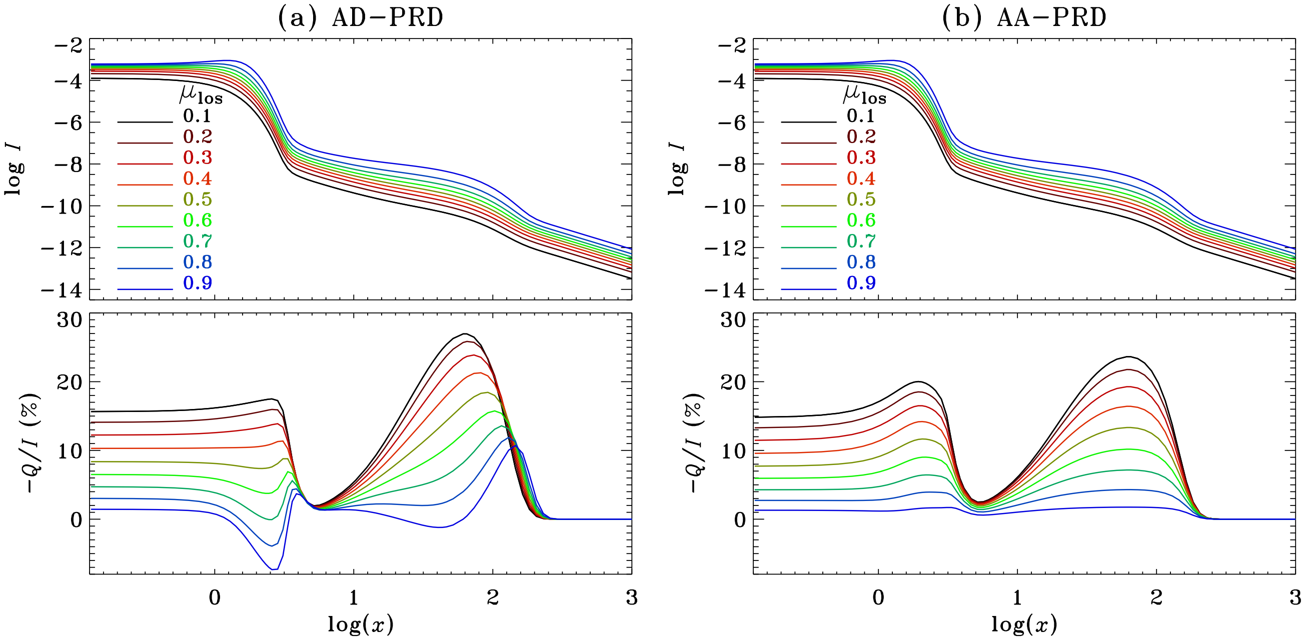

Figure 4. Same as Fig. 3, but for $R = 20$.

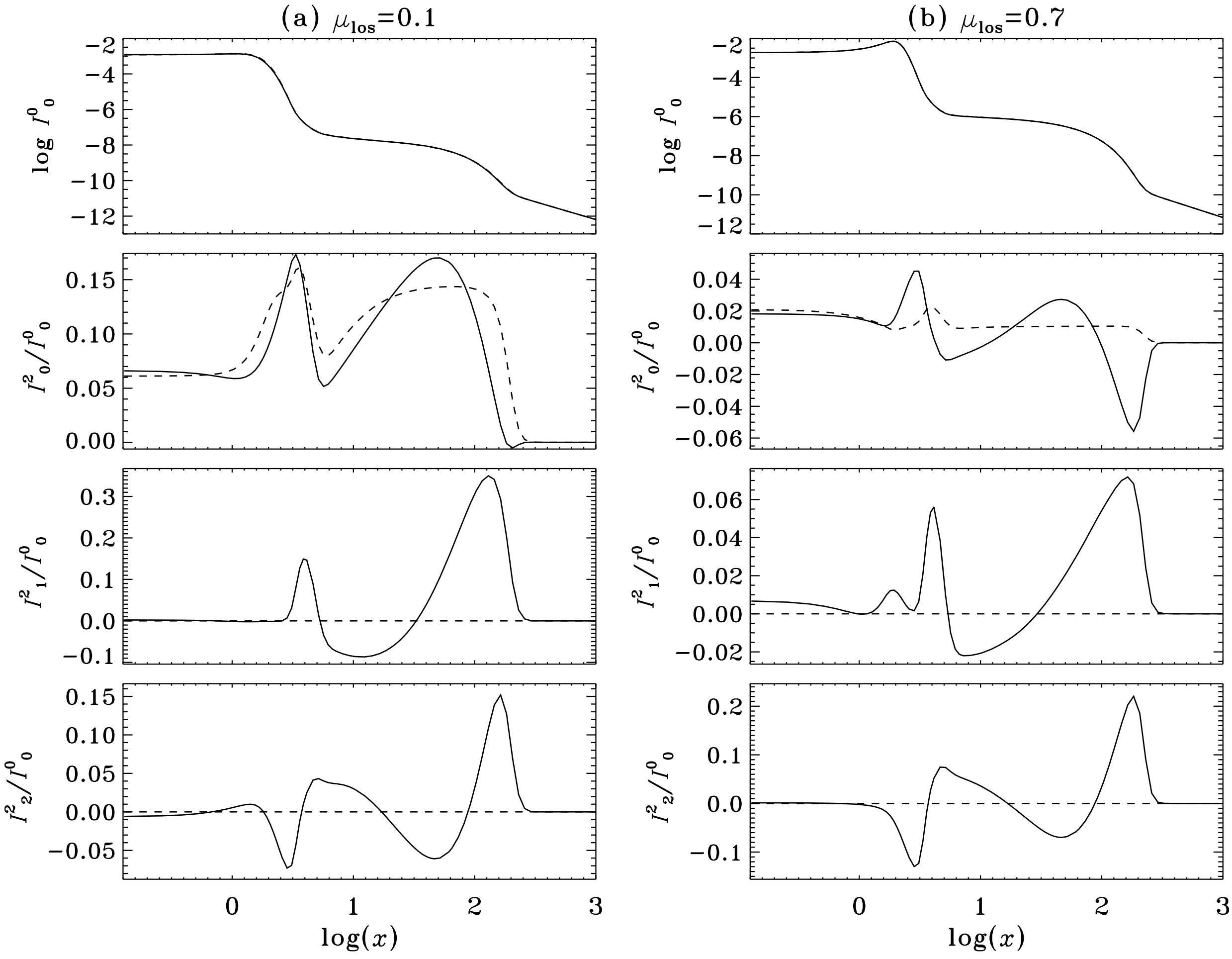

Figure 5. A comparison of the emergent $\mathcal{I}_0^0$ and $\mathcal{I}_Q^2/\mathcal{I}_0^0$ at $\mu_{\rm los} = 0.1$ (panel (a)) and $\mu_{\rm los} = 0.7$ (panel (b)) computed using AD-PRD (solid lines) and AA-PRD (dashed lines) functions. A spherically symmetric static medium with input parameters $R = 2$, $T = 100$, $\beta_c = 0$, $\beta_e = 10^{-5}$, $\epsilon = 10^{-4}$, $a = 10^{-3}$, and $\Gamma_{\rm E} = 0$ is considered.

$\mathcal{I}^K_Q$ components emerging at $\mu_{\rm los} = 0.1$ (panel (a)) and $\mu_{\rm los} = 0.7$ (panel (b)) for $R = 2$ and $T = 100$. In the case of AD-PRD, from equation (8) one readily obtains the following relation between the Stokes parameters and the irreducible components for the outgoing ray :

$$\begin{aligned} I(z, p, \nu) = {} & \mathcal{I}^0_0(z, p, \nu) + \frac{1}{2\sqrt{2}}(3\mu^2 - 1)\mathcal{I}^2_0(z, p, \nu) \\ & - \frac{\sqrt{3}}{2}\mu\sqrt{1-\mu^2}\mathcal{I}^2_1(z, p, \nu) \\ & + \frac{\sqrt{3}}{4}(1-\mu^2)\mathcal{I}^2_2(z, p, \nu), \qquad (28) \end{aligned}$$

$$\begin{aligned} Q(z, p, \nu) = {} & -\frac{3}{2\sqrt{2}}(1-\mu^2)\mathcal{I}^2_0(z, p, \nu) \\ & - \frac{\sqrt{3}}{2}\mu\sqrt{1-\mu^2}\mathcal{I}^2_1(z, p, \nu) \\ & - \frac{\sqrt{3}}{4}(1+\mu^2)\mathcal{I}^2_2(z, p, \nu). \qquad (29) \end{aligned}$$

For notational simplicity, we have suppressed the superscript '+' on the Stokes parameters as well as their irreducible components, which indicates the outgoing ray. Furthermore, the μ in the above equations represent $\mu(r, p)$ because these equations are valid for all the spherical shells that a given impact parameter ray p intersects along its path before it emerges from the outermost shell. In the case of AA-PRD, the only non-zero irreducible components are $\mathcal{I}^0_0$ and $\mathcal{I}^2_0$. The component $\mathcal{I}^0_0$ is essentially identical for AD-PRD and AA-PRD, while the other components show a significant difference (compare solid and dashed lines in Fig. 5). Since $\mathcal{I}^0_0$ is the dominant contributor to Stokes *I* (see equation 28), the latter is insensitive to AD-PRD or AA-PRD. On the other hand the Stokes *Q* is composed of three components $\mathcal{I}^2_Q$ with $Q = 0, 1, 2$ (see equation 29). When $\mu_{\rm los} = \mu(R, p)$ is small (namely, close to the limb), only $\mathcal{I}^2_0$ and $\mathcal{I}^2_2$ contribute. However, the dominant contribution comes from $\mathcal{I}^2_0$. On the other hand, when $\mu_{\rm los}$ is large $\mathcal{I}^2_1$ also contributes resulting in relatively larger difference between *Q*/*I* computed with AD-PRD and AA-PRD.

4.2 Dependence on electron scattering opacity β_e

In Fig. 6, we illustrate the dependence of the differences between the *Q*/*I* computed with AD-PRD (panel (a)) and AA-PRD (panel (b)) on the electron scattering opacity parametrized as β_e. The corresponding error as defined in equation (27) is shown in panel (c). Since the differences between AD-PRD and AA-PRD solutions are mainly seen in the *Q*/*I* profiles, we do not present the corresponding intensity profiles (also in the next subsection). We have considered $R = 2$ and $T = 100$ for this purpose. As in Sampoorna, Megha & Supriya (2022), we have varied β_e from 10^{-8} to 10^{-3} in steps of one dex. The *Q*/*I* profiles for $\beta_e = 0$ are also shown. The influence of varying β_e on the *Q*/*I* profiles is similar for both AD-PRD and AA-PRD cases, and has been described in detail in Sampoorna, Megha & Supriya (2022). For the optically thin case considered here, the effect of varying β_e is mainly seen in the far wings, namely in and around the secondary peak. Only for β_e as large as 10^{-3} the influence of electron scattering redistribution is seen in the line core and near wing PRD peak. Thus the differences between AD-PRD and AA-PRD are nearly independent of β_e in the line core and near wing PRD peak, which is also reflected in the error $\Delta(Q/I)$ (see panel (c) of Fig. 6), except for $\beta_e = 10^{-3}$ (see the blue line in panel (c) of Fig. 6). On the other hand, the differences between AD-PRD and AA-PRD in and around the secondary peak in *Q*/*I* shows a strong dependence on β_e. This difference in general increases with β_e as also reflected in $\Delta(Q/I)$ (see panel (c) of Fig. 6). For example, while the secondary peak in *Q*/*I* computed with AA-PRD exhibits flat topped profile shape for $\beta_e = 10^{-4}$, the corresponding AD-PRD case exhibits a more rounded profile shape (compare purple lines in panels (a) and (b) of Fig. 6).

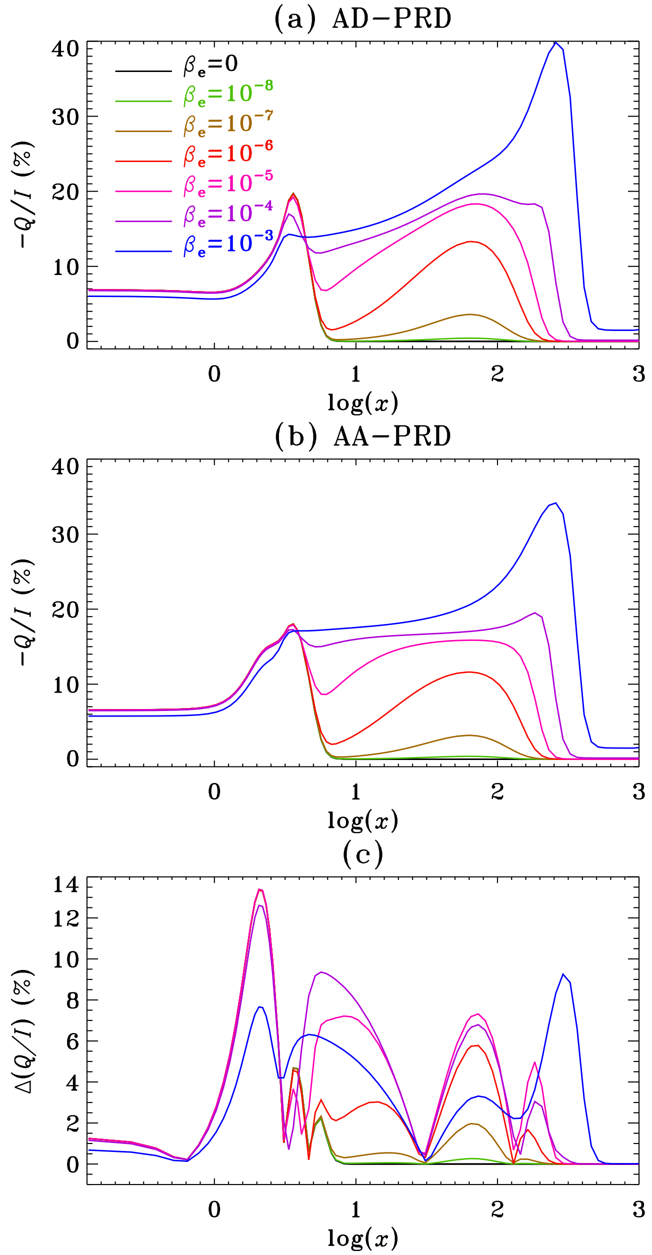

Figure 6. A comparison of the fractional linear polarization *Q*/*I* profiles at $\mu_{\rm los} = 0.1$ computed using AD-PRD (panel (a)) and AA-PRD (panel (b)) functions for varying values of β_e. Panel (c) shows the corresponding error $\Delta(Q/I)$ in percentage (see equation 27). A spherically symmetric static medium with input parameters $R = 2$, $T = 100$, $\beta_c = 0$, $\epsilon = 10^{-4}$, $a = 10^{-3}$, and $\Gamma_{\rm E} = 0$ is considered. Different lines correspond to a different value of β_e and are indicated in panel (a), which remain valid for both the panels (b) and (c).

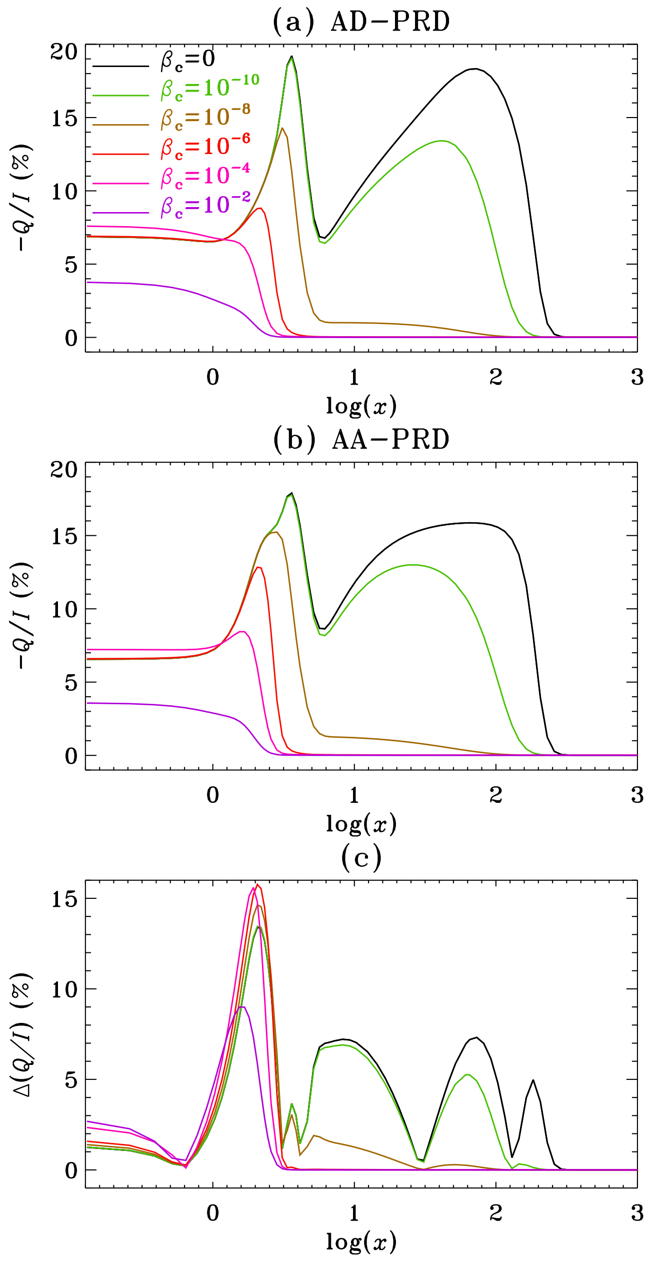

Figure 7. A comparison of the fractional linear polarization *Q*/*I* profiles at $\mu_{\rm los} = 0.1$ computed using AD-PRD (panel (a)) and AA-PRD (panel (b)) functions for varying values of β_c. Panel (c) shows the corresponding error $\Delta(Q/I)$ in percentage (see equation 27). A spherically symmetric static medium with input parameters $R = 2$, $T = 100$, $\beta_e = 10^{-5}$, $\epsilon = 10^{-4}$, $a = 10^{-3}$, and $\Gamma_{\rm E} = 0$ is considered. Different lines correspond to a different value of β_c and are indicated in panel (a), which remain valid for both the panels (b) and (c).

4.3 Dependence on continuum parameter β_c

For $R = 2$ and $T = 100$, we illustrate in Fig. 7, the dependence of the differences between the *Q*/*I* computed with AD-PRD (panel (a)) and AA-PRD (panel (b)) on the background continuum parameter β_c. The corresponding error (see equation 27) is shown in panel (c). We have varied β_c from 10^{-10} to 10^{-2} in steps of two dex. The *Q*/*I* profiles for the pure line case ($\beta_c = 0$) are also shown. Since the background continuum is assumed to be unpolarized, it drives the polarization towards zero at frequencies where the continuum opacity dominates over the line and electron scattering opacities. As β_c increases, this occurs at progressively smaller frequency, thereby confining the *Q*/*I* profiles to smaller frequency bandwidths around the line core region. Therefore, in the far wings (namely, in and around the secondary peak in *Q*/*I*) the differences between AD-PRD and AA-PRD decreases with β_c (see panel (c) in Fig. 7). However, surprisingly in the region close to the line centre the differences slightly increase with β_c, while at the near wing PRD peak differences initially increase until $\beta_c = 10^{-6}$ and then decreases (see e.g. red and purple coloured lines in panel (c) of Fig. 7). This clearly shows the importance of including AD-PRD effects even when the background continuum parameter is as large as $\beta_c = 10^{-2}$.

4.4 Impact of velocity field

A comparison of emergent Stokes profiles computed with AD-PRD (solid lines) and AA-PRD (dashed lines) in the presence of radial velocity fields is shown in Figs 8 and 9 for $T = 100$ and $R = 2$ (panel (a)), 20 (panel (b)), and 200 (panel (c)). Since the velocity field introduces asymmetries, the Stokes profiles are shown for both positive and negative values of the non-dimensional frequency x. Both the above-mentioned figures are identical, except for the choice of frequency range for the abscissa. A larger frequency bandwidth is used for Fig. 8 to display the far wing region where the electron scattering dominates, while a smaller frequency bandwidth is used for Fig. 9 to display the line core and near wing regions where the atomic scattering dominates. The velocity field is given by an arctan velocity law (see e.g. Mihalas, Kunasz & Hummer 1975, 1976) of the form

$$V(r) = V_{\rm max}\left[\tan^{-1}(ar+b) - \tan^{-1}(a+b)\right], \qquad (30)$$

with a maximum expansion velocity $V_{\rm max}$ of two mean thermal units. Following Mihalas, Kunasz & Hummer (1975), we have chosen the radius $r_v(= -b/a)$ at which the maximum velocity gradient occurs to be at $(R + 1)/2$ and the parameter a such that we have one characteristic width of the velocity function (namely, $a(r_v - 1) = 1$).

The effect of the velocity fields on the emergent *I* and *Q*/*I* profiles are identical to those discussed in section 3.3 of Sampoorna, Megha & Supriya (2022), and hence we do not repeat them here. Primarily, the velocity fields give rise to *I* and *Q*/*I* profiles that are asymmetric about the line centre. For the optically thin case considered here, the asymmetry in *Q*/*I* profiles is more apparent for all the different outer radius *R* unlike the *I* profiles (see Figs 8 and 9). Furthermore, the influence of electron scattering on *I* and *Q*/*I* profiles emanating from a moving spherical medium is similar to the corresponding static case, namely, an enhancement of the intensity in the wings and generation of a secondary peak in the *Q*/*I* profiles. The secondary peak is, however, asymmetric for the moving case (see Fig. 8). The nature of the differences between the AA-PRD and AD-PRD solutions is also similar to the corresponding static case (compare Figs 2 and 8). However, the overall error $\Delta(Q/I)$ is somewhat smaller for the moving medium than the corresponding static spherical medium (compare the bottom rows of Figs 2 and 8).

5 CONCLUSIONS

In this paper, we investigate the impact of AD-PRD on resonance line polarization emerging from a spherically symmetric extended and expanding medium. We account for both scattering of line photons by atoms and electrons. To numerically solve this problem, we apply an accelerated lambda iteration method (Hauschildt &

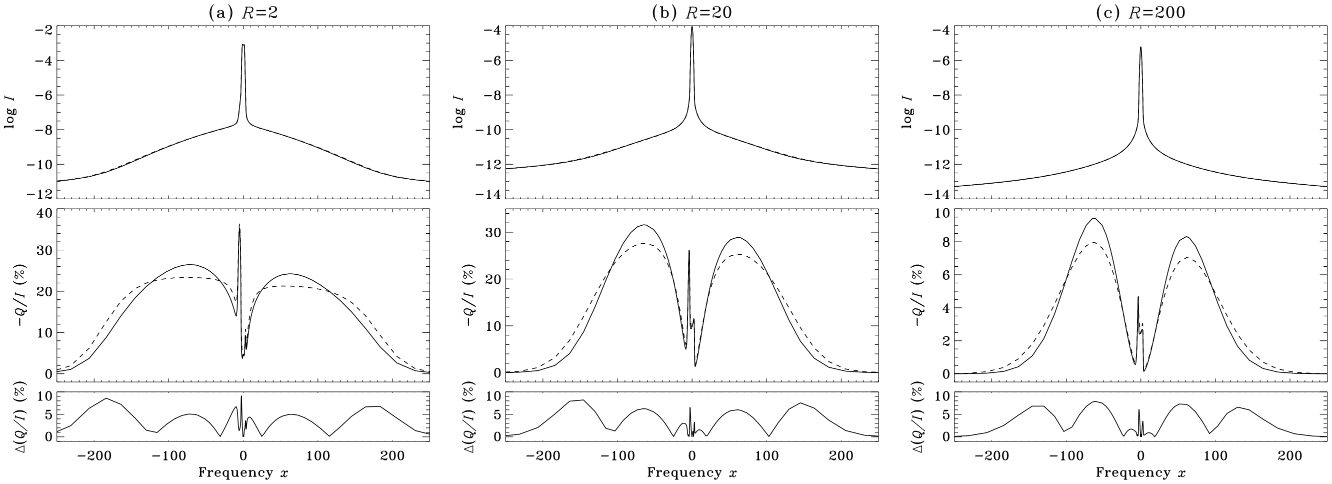

Figure 8. A comparison of the emergent Stokes *I* and fractional linear polarization *Q*/*I* profiles at $\mu_{\rm los} = 0.1$ computed using AD-PRD (solid lines) and AA-PRD (dashed lines) functions. Bottom row displays the corresponding error $\Delta(Q/I)$ in percentage (see equation 27). A spherically symmetric moving medium with input parameters $T = 100$, $\beta_c = 0$, $\beta_e = 10^{-5}$, $\epsilon = 10^{-4}$, $a = 10^{-3}$, and $\Gamma_{\rm E} = 0$ is considered. Panels (a), (b), and (c) correspond, respectively, to $R = 2$, 20, and 200. For the velocity field we have used an arctan velocity law with a maximum expansion velocity of two mean thermal units.

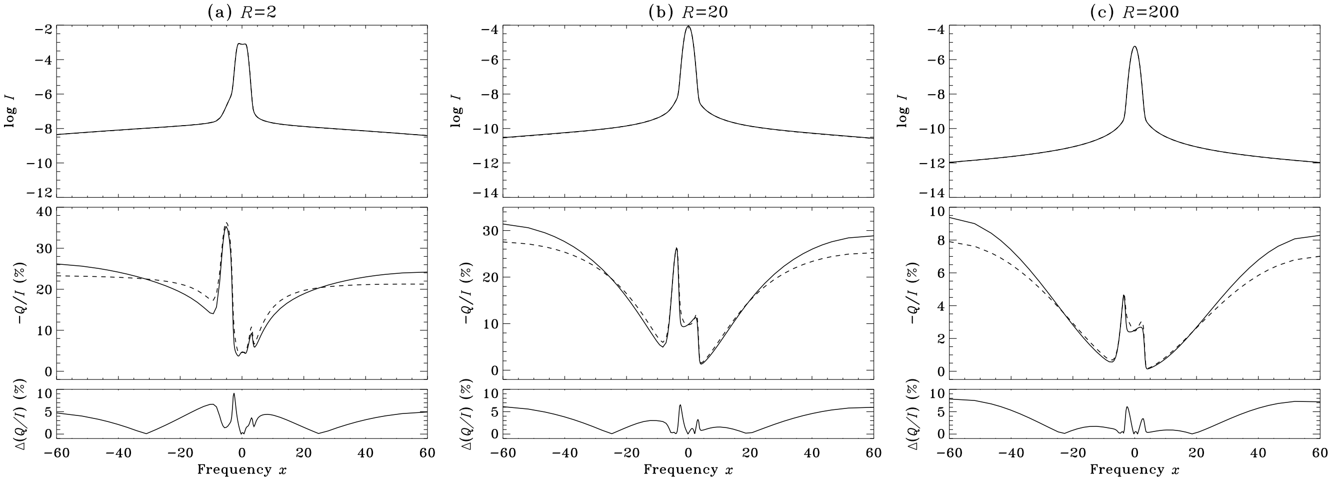

Figure 9. Same as Fig. 8. However, the profiles are shown for a shorter frequency range to better resolve the region in and around the line core and near wings.

Baron 2004) as well as a scattering expansion method (Frisch et al. 2009). These numerical schemes are applied to the CMF polarized transfer equation in the irreducible spherical tensorial representation (Frisch 2010). In this approach, the Stokes and source vectors are decomposed into their irreducible components and the AD-PRD functions are expanded over the azimuth difference of the incoming and outgoing radiation using a cosine Fourier series. The scattering expansion method is computationally more advantageous than the ALI method. This is in particular true for transfer in spherical medium, where the spatial and angle grids are coupled as we solve the concerned transfer problem in the (p, z) coordinate system (Hummer & Rybicki 1971).

Despite using the scattering expansion method, the heavy computational requirements have limited us to consider optically thin isothermal spherical medium with inverse square law opacity distribution. For our studies, we have considered different extension *R* of the spherical medium with $R = 2$, 20, and 200, and line integrated radial optical thickness of $T = 10$ and 100. In this region of parameter space, the linear polarization *Q*/*I* is highly sensitive to the choice of the redistribution function, namely AD-PRD or AA-PRD (see Figs 1 and 2). Significant differences between *Q*/*I* computed with AD-PRD and AA-PRD are seen in both amplitude and shape in the near wing PRD peak (which arises due to type-II atomic scattering) and the secondary peak (which arises due to electron scattering redistribution). Noticeable differences in the amplitude of *Q*/*I* in the line core region is also seen. Because of the spherical nature of the problem, the AD-PRD effects on *Q*/*I* are relatively larger for a line of sight close to the disc centre than near the limb (see Figs 3 and 4). We have also shown that when the contribution of electron scattering increases, the differences between *Q*/*I* computed with AD-PRD and AA-PRD at the secondary peak in general also increases (see Fig. 6). However, when the contribution from the background continuum is added, these differences decrease since the secondary peak significantly decreases with increasing values of β_c (see Fig. 7). On the other hand the differences around the line core and near wing PRD peak somewhat increases. In the presence of a non-zero radial velocity field, the effects of AD-PRD on *Q*/*I* are similar to the corresponding static case, but the error $\Delta(Q/I)$ is relatively smaller. From these numerical studies, we therefore conclude that AD-PRD effects have to be included for modelling the linear polarization profiles of optically thin lines emanating from spherically symmetric extended and expanding media, although such calculations are computationally expensive.

ACKNOWLEDGEMENTS

We acknowledge the use of the high-performance computing facility at the Indian Institute of Astrophysics. MS acknowledges the support from the Science and Engineering Research Board (SERB), Department of Science and Technology, Government of India via a SERB-Women Excellence Award research grant WEA/2020/000012. We thank the referee for helpful comments that improved the presentation of the paper.

DATA AVAILABILITY

The data underlying this article will be shared on reasonable request to the corresponding author.

REFERENCES

Anusha L. S., 2023, ApJ, 949, 84

Anusha L. S., Nagendra K. N., 2012, ApJ, 746, 84

Benedusi P., Janett G., Riva S., Krause R., Belluzzi L., 2022, A&A, 664, A197

Benedusi P., Riva S., Zulian P., Štěpán J., Belluzzi L., Krause R., 2023, J. Comput. Phys., 479, 112013

Bommier V., 1997a, A&A, 328, 706

Bommier V., 1997b, A&A, 328, 726

Cannon C. J., 1973, ApJ, 185, 621

Chandrasekhar S., 1950, Radiative Transfer. Clarendon Press, Oxford

del Pino Alemán T., Trujillo Bueno J., Casini R., Manso Sainz R., 2020, ApJ, 891, 91

Domke H., Hubeny I., 1988, ApJ, 334, 527

Dumont S., Omont A., Pecker J. C., Rees D., 1977, A&A, 54, 675

Faurobert M., 1987, A&A, 178, 269

Faurobert M., 1988, A&A, 194, 268

Frisch H., 2009, in Berdyugina S. V., Nagendra K. N., Ramelli R., eds, ASP Conf. Ser. Vol. 405, Solar Polarization 5: In Honor of Jan Stenflo. Astron. Soc. Pac., San Francisco, p. 87

Frisch H., 2010, A&A, 522, A41

Frisch H., Anusha L. S., Sampoorna M., Nagendra K. N., 2009, A&A, 501, 335

Hauschildt P. H., Baron E., 2004, A&A, 417, 317

Hubeny I., Mihalas D., 2015, Theory of Stellar Atmospheres: An Introduction to Astrophysical Non-equilibrium Quantitative Spectroscopic Analysis. Princeton University Press, Princeton, NJ

Hummer D. G., 1962, MNRAS, 125, 21

Hummer D. G., Rybicki G. B., 1971, MNRAS, 152, 1

Janett G., Alsina Ballester E., Guerreiro N., Riva S., Belluzzi L., del Pino Alemán T., Trujillo Bueno J., 2021, A&A, 655, A13

Landi Degl'Innocenti E., Landolfi M., 2004, Polarization in Spectral Lines. Kluwer, Dordrecht

Megha A., Sampoorna M., Nagendra K. N., Anusha L. S., Sankarasubramanian K., 2019, ApJ, 879, 48

Megha A., Sampoorna M., Nagendra K. N., Anusha L. S., Sankarasubramanian K., 2020, ApJ, 903, 6

Mihalas D., 1978, Stellar Atmospheres. W.H. Freeman, San Francisco

Mihalas D., Kunasz P. B., Hummer D. G., 1975, ApJ, 202, 465

Mihalas D., Kunasz P. B., Hummer D. G., 1976, ApJ, 210, 419

Nagendra K. N., 2019a, in Werner K., Stehle C., Rauch T., Lanz T., eds, ASP Conf. Ser. Vol. 519, Radiative Signatures from the Cosmos. Astron. Soc. Pac., San Francisco, p. 51

Nagendra K. N., 2019b, in Belluzzi L., Casini R., Romoli M., Trujillo Bueno J., eds, ASP Conf. Ser. Vol. 526, Solar Polarization Workshop 8. Astron. Soc. Pac., San Francisco, p. 99

Nagendra K. N., Sampoorna M., 2011, A&A, 535, A88

Nagendra K. N., Sampoorna M., 2012, ApJ, 757, 33

Nagendra K. N., Frisch H., Faurobert M., 2002, A&A, 395, 305

Nagendra K. N., Sowmya K., Sampoorna M., Stenflo J. O., Anusha L. S., 2020, ApJ, 898, 49

Olson G. L., Kunasz P. B., 1987, J. Quant. Spectrosc. Radiat. Transfer, 38, 325

Olson G. L., Auer L. H., Buchler J. R., 1986, J. Quant. Spectrosc. Radiat. Transfer, 35, 431

Riva S., Guerreiro N., Janett G., Rossinelli D., Benedusi P., Krause R., Belluzzi L., 2023, A&A, in press

Sampoorna M., 2014, in Nagendra K. N., Stenflo J. O., Qu Z. Q., Sampoorna M., eds, ASP Conf. Ser. Vol. 489, Solar Polarization 7. Astron. Soc. Pac., San Francisco, p. 197

Sampoorna M., Nagendra K. N., 2015a, in Nagendra K. N., Bagnulo S., Centeno R., Jesús Martínez González M., eds, Proc. IAU Symp. 305, Polarimetry: From the Sun to Stars and Stellar Environments. Kluwer, Dordrecht, p. 387

Sampoorna M., Nagendra K. N., 2015b, ApJ, 812, 28

Sampoorna M., Nagendra K. N., Stenflo J. O., 2008, ApJ, 679, 889

Sampoorna M., Nagendra K. N., Frisch H., 2011, A&A, 527, A89

Sampoorna M., Nagendra K. N., Stenflo J. O., 2017, ApJ, 844, 97

Sampoorna M., Nagendra K. N., Sowmya K., Stenflo J. O., Anusha L. S., 2019, ApJ, 883, 188

Sampoorna M., Megha A., Supriya H. D., 2022, ApJ, 937, 25

Stenflo J. O., 1994, Solar Magnetic Fields - Polarized Radiation Diagnostics. Kluwer, Dordrecht

Supriya H. D., Nagendra K. N., Sampoorna M., Ravindra B., 2012, MNRAS, 425, 527

Supriya H. D., Sampoorna M., Nagendra K. N., Ravindra B., Anusha L. S., 2013a, J. Quant. Spectrosc. Radiat. Transfer, 119, 67

Supriya H. D., Smitha H. N., Nagendra K. N., Ravindra B., Sampoorna M., 2013b, MNRAS, 429, 275

Trujillo Bueno J., 2003, in Hubeny I., Mihalas D., Werner K., eds, ASP Conf. Ser. Vol. 288, Stellar Atmosphere Modeling. Astron. Soc. Pac., San Francisco, p. 551

This paper has been typeset from a TEX/LATEX file prepared by the author.